

COVER PAGE

Document downloaded by @DAEL

Thu Nov 26 23:59:41 2026
For personal use

When automatic English translation is provided, only the original document is authentic.
The EAA cannot be held responsible of any translation error

Bibliographical reference

Practical Computational Aeroacoustics for Compact Surfaces in Low Mach Number Flows, Ainara Pradera-Mallabiabarrena, Graeme Keith, Finn Jacobsen, Alejandro Rivas and Nere Gil-Negrete, Acta Acustica **vol. 97** (Number 1), 2011, pp. 14-23

DOI
https://doi.org/10.3813/AAA.918382

ACTA ACUSTICA UNITED WITH ACUSTICA
Vol. 97 (2011) 14 – 23

DOI 10.3813/AAA.918382

Practical Computational Aeroacoustics for Compact Surfaces in Low Mach Number Flows

Ainara Pradera-Mallabiabarrena[1,3], Graeme Keith[2], Finn Jacobsen[3], Alejandro Rivas[4], Nere Gil-Negrete[1]

[1] CEIT and Tecnun-University of Navarra, Manuel de Lardizábal 15, 20018 San Sebastián, Spain. apradera@ceit.es

[2] Lloyd's Register ODS, Titangade 15, 2200 Copenhagen N, Denmark

[3] Acoustic Technology, Department of Electrical Engineering, Technical University of Denmark, Ørsteds Plads B352, 2800 Lyngby, Denmark

[4] Tecnun-University of Navarra, Manuel de Lardizábal 13, 20018 San Sebastián, Spain

Summary

Sound generation has been widely studied using numerical hybrid methods. The aim of this paper is to introduce a flexible procedure where the acoustic source data may be synthesized and stored from commercially available Computational Fluid Dynamics (CFD) codes and later used to predict radiated noise. Different applications will require either analytical or numerical methods for the radiation calculations. Attention is restricted to low Mach number flows where the noise generation is dominated by the interaction of the flow with a surface with at least one characteristic dimension short compared to the wavelength of interest. This makes it possible to focus on the surface source term of the Ffowcs Williams-Hawkings equation. In this paper, in order to illustrate the basic method for storing and utilizing data from the CFD analysis, the flow past a circular cylinder at a Reynolds number of $\mathrm{Re} = 1.4 \cdot 10^5$ will be studied, where the cylinder is compact and therefore the analytical free-space Green's function may be used.

PACS no. 43.28.Ra

1. Introduction

Computational Aeroacoustics (CAA) has come of age. The relentless advance of processor performance and imaginative and carefully optimized numerical methods have made it not only possible, but in some cases practicable to predict the noise generated by unsteady flow using purely computational means. Approaches range from Direct Numerical Simulation (DNS) of the unsteady compressible flow, including the radiated acoustic waves themselves [1, 2, 3], through DNS of the unsteady flow coupled with an appropriate form of the acoustic analogy (either Lighthill's original [4, 5] or some of its more recent descendants e.g. [6]) to predict the radiated acoustic field [7, 2]. Various combinations of Large Eddy Simulation (LES), Detached Eddy Simulation (DES) and Unsteady Reynolds-Averaged Navier-Stokes (URANS) turbulence modelling have been used to lighten the computational burden [8, 9, 10], again both directly predicting the radiated field [11, 12, 13, 14] and in combination with one or other form of the acoustic analogy [15, 16, 17].

Notwithstanding this burgeoning development, the adoption of CAA in practice has been relatively restricted outside of aeronautical applications and parts of the automotive industry. This is due to a number of factors, but two of the primary obstacles have been the need for bespoke code, unavailable or inaccessible to ordinary acoustic practitioners, and persistent expense, in terms of both modelling and computation time, that, in spite of recent improvements, is still too punitive for most applications. These impediments make CAA a less attractive option, particularly when semi-empirical methods can be used with at least as great if not rather better accuracy.

Much of the expense of CAA arises from the need to carry out unsteady CFD calculations. Methods by which noise source information can be reconstructed from *steady* CFD results are an attempt to circumvent this problem [18, 19, 20, 21]. Typically the assumptions that go into these noise source reconstruction methods are quite restrictive and they can, in theory, only be applied in situations for which results are known in advance. Nonetheless, employed cautiously and interpreted wisely they can provide a useful practical tool for the relative evaluation of certain flows' efficacy to generate noise. A more versatile approach, though nonetheless still rather restricted in its application, is based on combining CFD with normal mode analysis [22, 23], wherein steady CFD calculations can be used to predict mean flows, whose spatio-temporal stability characteristics can be used to predict

Received 7 April 2010,
accepted 8 September 2010.

© S. Hirzel Verlag · EAA

frequency and (hydrodynamic) wavelength information, which in turn can be synthesized to give far field radiated noise [24, 25]. Yet once more, these methods require purpose-designed code, as well as a fairly in depth knowledge of the methods, and until they are developed to become more accessible, they are unlikely to catch on in widespread practical application.

Until then the costs associated with unsteady calculations must be accepted and work needs to be done to find ways of facilitating the utilization of these results for the practicable prediction of radiated noise. This paper introduces a versatile framework in which CFD results acquired using commercially available CFD codes may be synthesized, stored and then used to predict radiated noise. The radiation calculations may employ purely analytical methods or numerical methods depending on the application. In the latter case, the numerical acoustic calculations should be carried out in commercially available numerical acoustics software. Practical imperatives demand that the storage requirements of the method are no greater than necessary and entreat that CFD calculations should not need to be repeated in the event that different acoustic scenarios should be investigated while the flow remains essentially the same.

This paper develops the framework in the context of a simple example, the noise generated by the flow past a circular cylinder. Future work will show how these basic ideas can be extended to more complex scattering geometries requiring numerical acoustic solutions. Attention is restricted to low Mach number flows where the noise generation is dominated by the interaction of the flow with a surface at least one of whose typical dimensions is short compared to the wavelength of interest. This restriction allows to concentrate on the surface source term of the Ffowcs Williams-Hawkings equation, which is the source term that dominates in a large range of practical applications [26].

2. Model

Low Mach number flow past a fixed impermeable surface, Σ, is considered. This surface will be taken to be compact, i.e. characterized by a length scale that is small compared to an acoustic wavelength over the frequency range of interest. Moreover, it will be assumed the fluctuating pressure on the surface Σ can be calculated using CFD and is given.

There may be other surfaces in the vicinity of Σ that are not compact and whose main role in the generation and propagation of noise is to scatter the noise generated by the interaction of the flow with the compact surface Σ. This configuration covers many examples of practical interest including the ubiquitous wing mirror, where the mirror itself is compact and the car body mainly acts to scatter the noise generated by the interaction of the flow with the wing mirror. Further examples include obstructions in ducts, such as orifice plates and valves in which the duct walls play only a inconsequential role in the production of noise, but are instrumental in the radiation and propagation; the noise is generated by the interaction of the flow with the obstruction. See, for example, [27].

The generation of noise is modelled using a reduced version of the Ffowcs Williams–Hawkings equation for a fixed impermeable surface in a low Mach number homentropic flow [28]

$$\left(\frac{1}{c_0^2}\frac{\partial^2}{\partial t^2} - \nabla^2\right)\left\{H\left[h(\mathbf{x})\right]p(\mathbf{x},t)\right\} = \frac{\partial^2}{\partial x_i \partial x_j}\left\{H\left[h(\mathbf{x})\right]\rho u_i u_j\right\} - \frac{\partial}{\partial x_j}\left\{p(\mathbf{x},t)\frac{\partial h(\mathbf{x})}{\partial x_j}\delta\left[h(\mathbf{x})\right]\right\}. \quad (1)$$

Here H is the Heaviside step function, δ the Dirac delta function and c_0 the isentropic sound speed of the fluid at rest. The function $h(\mathbf{x})$ describes the surface Σ in that $h = 0$ on Σ, $h < 0$ for $\mathbf{x}$ in the interior of Σ and $h > 0$ in the exterior of Σ, i.e. in the flow. Equation (1) is a rearrangement of the Navier-Stokes equations (in this case in an inviscid and homentropic limit) that isolates the quantity $H[h(\mathbf{x})]p(\mathbf{x},t)$, which is the fluid pressure restricted to the fluid and zero in the interior of Σ. As such it is valid everywhere, inside and outside Σ and no further account of the conditions on the surface Σ is required. The surface is effectively replaced by the source distribution given by the second term on the right hand side of equation (1), which is restricted to the surface by the delta function.

Far away from the surface Σ, the quantity $H[h(\mathbf{x})] \cdot p(\mathbf{x},t) = p(\mathbf{x},t)$ is simply the acoustic pressure and equation (1) formally resembles a forced wave equation, albeit with the pressure for which it is being solved appears both explicitly and implicitly in the forcing terms on the right hand side. This formulation is useful because the magnitude of the source terms falls rapidly with distance compared with the acoustic pressure so the flow need only be calculated in a relatively small region outside of which the source terms are negligible. The far-field acoustic pressure can then be calculated by inverting equation (1) with the right hand side given by the direct calculation.

Elementary aeroacoustic theory tells that in the presence of a compact surface, i.e. one with characteristic length scales short compared to an acoustic wavelength, the contribution from the second source term on the right hand side of equation (1) dominates the far-field acoustic pressure. This is also the case if there are, in addition, large flat surfaces in the vicinity of Σ as described above. Their effect can be thought of as effectively introducing an image source distribution with similar properties to the original source distribution, including the priority of the second surface term.

The approach of this research work is to treat compact surfaces by replacing them with source distributions using the Ffowcs Williams–Hawkings formulation, calculating the pressure on the surface using CFD. Non-compact surfaces, whose primary effect is to scatter the noise generated by the interaction of the flow with the compact surface, will be managed by using Green's functions that satisfy the boundary condition on these surfaces. In this paper, in order to illustrate the basic method for storing and

utilizing data from the CFD analysis, attention will be restricted to free-field applications where the only surfaces are compact so that the (analytical) free-space Green's function may be used.

3. Analysis

The result of the foregoing discussion is that the equation to be solved is

$$\left(\frac{1}{c_0^2}\frac{\partial^2}{\partial t^2} - \nabla^2\right)\left\{H\left[h(\mathbf{x})\right]p(\mathbf{x},t)\right\} = -\frac{\partial}{\partial x_j}\left\{P(\mathbf{x},t)\frac{\partial h(\mathbf{x})}{\partial x_j}\delta\left[h(\mathbf{x})\right]\right\}, \quad (2)$$

where $P(\mathbf{x},t)$ is taken to be given (calculated from the CFD). This is solved by convolution with a Green's function $G(\mathbf{x},\mathbf{y};t-\tau)$ that satisfies

$$\left(\frac{1}{c_0^2}\frac{\partial^2}{\partial t^2} - \nabla^2\right)G(\mathbf{x},\mathbf{y};t-\tau) = \delta(\mathbf{x}-\mathbf{y})\,\delta(t-\tau), \quad (3)$$

together with boundary conditions on scattering surfaces and appropriate radiation or causality conditions. Integrating by parts moves the derivative on the source term over the Green's function

$$\begin{aligned} &H\left[h(\mathbf{x})\right]p(\mathbf{x},t) \\ &= \int_{-\infty}^{\infty}\int_V P(\mathbf{y},\tau)\frac{\partial}{\partial y_j}G(\mathbf{x},\mathbf{y};t-\tau)\frac{\partial h(\mathbf{x})}{\partial y_j}\delta\left[h(\mathbf{x})\right]\mathrm{d}^3\mathbf{y}d\tau \\ &= \int_{-\infty}^{\infty}\int_\Sigma P(\mathbf{y},\tau)\,n_j\frac{\partial}{\partial y_j}G(\mathbf{x},\mathbf{y};t-\tau)\,\mathrm{d}^2\mathbf{y}d\tau, \end{aligned} \quad (4)$$

where $\mathbf{n}$ is the unit normal to the surface Σ pointing into the fluid.

A frequency domain Green's function is defined,

$$g(\mathbf{x},\mathbf{y},\omega) = \int_{-\infty}^{\infty} G(\mathbf{x},\mathbf{y};t-\tau)\mathrm{e}^{-\mathrm{i}\omega(t-\tau)}\mathrm{d}t, \quad (5)$$

so $g(\mathbf{x},\mathbf{y},\omega)$ satisfies

$$\left(\nabla^2 + k^2\right)g(\mathbf{x},\mathbf{y},\omega) = -\delta(\mathbf{x}-\mathbf{y}), \quad (6)$$

with $k = \omega/c_0$. By Fourier inversion,

$$G(\mathbf{x},\mathbf{y},t-\tau) = \frac{1}{2\pi}\int_{-\infty}^{\infty} g(\mathbf{x},\mathbf{y};\omega)\,\mathrm{e}^{\mathrm{i}\omega(t-\tau)}\mathrm{d}\omega. \quad (7)$$

Substituting equation (7) into equation (4) and rearranging the order of integration reveals that $H[h(\mathbf{x})]p(\mathbf{x},t)$ is the inverse Fourier transform of

$$\tilde{p}(\mathbf{x},\omega) = \int_\Sigma \tilde{P}(\mathbf{y},\omega)n_j\frac{\partial}{\partial y_j}g(\mathbf{x},\mathbf{y},\omega)\mathrm{d}^2\mathbf{y}. \quad (8)$$

The surface Σ is now divided into a number of small elements, which are labeled Σ_l,

$$\begin{aligned} \tilde{p}(\mathbf{x},\omega) &= \sum_l \int_{\Sigma_l} \tilde{P}(\mathbf{y},\omega)\,n_j\frac{\partial}{\partial y_j}g(\mathbf{x},\mathbf{y},\omega)\,\mathrm{d}^2\mathbf{y} \\ &\approx \sum_l \int_{\Sigma_l} \tilde{P}(\mathbf{y},\omega)n_j\frac{\partial g}{\partial y_j}\left(\mathbf{x},\mathbf{y}^l,\omega\right)\mathrm{d}^2\mathbf{y}, \end{aligned} \quad (9)$$

where $\mathbf{y}^l$ denotes the value of $\mathbf{y}$ at the centre of the l^{th} element Σ_l. Clearly the element size should be chosen so that the (derivative of the) Green's function does not vary significantly over a single element, i.e. the element size should be small compared to an acoustic wavelength. Moreover, in most cases, this approximation will require that $|\mathbf{x}| \gg |\mathbf{y}|$. These restrictions may be relaxed by formally expanding the Green's function and calculating higher order moments of the pressure on the surface, but this issue shall not be explored further in this paper.

In the event that the elements are small compared to their curvature so that variations in $\mathbf{n}$ can also be ignored then

$$\begin{aligned} \tilde{p}(\mathbf{x},\omega) &\approx \sum_l \int_{\Sigma_l} \tilde{P}(\mathbf{y},\omega)\,\mathrm{d}^2\mathbf{y} \times n_j\left(\mathbf{y}^l\right)\frac{\partial g}{\partial y_j}\left(\mathbf{x},\mathbf{y}^l,\omega\right) \\ &\equiv f_l(\omega)\gamma_l(\mathbf{x},\omega), \end{aligned} \quad (10)$$

where

$$\begin{aligned} f_l(\omega) &= \sum_l \int_{\Sigma_l} \tilde{P}(\mathbf{y},\omega)\,\mathrm{d}^2\mathbf{y}, \\ \gamma_l(\mathbf{x},\omega) &= \sum_l n_j\left(\mathbf{y}^l\right)\frac{\partial g}{\partial y_j}\left(\mathbf{x},\mathbf{y}^l,\omega\right). \end{aligned} \quad (11)$$

The power spectral density $\Pi(\mathbf{x},\omega)$ of the acoustic pressure is then given by (see chapter 3 in [29])

$$\begin{aligned} &\Pi(\mathbf{x},\omega)\delta\left(\omega-\omega'\right) \\ &= \left\langle\widetilde{p}(\mathbf{x},\omega)\widetilde{p}^*\left(\mathbf{x},\omega'\right)\right\rangle \\ &= \gamma_l(\mathbf{x},\omega)\left\langle f_l(\omega)f_m^*\left(\omega'\right)\right\rangle\gamma_m^*\left(\mathbf{x},\omega'\right) \\ &= \gamma_l(\mathbf{x},\omega)\Phi_{lm}(\omega)\delta\left(\omega-\omega'\right)\gamma_m^*\left(\mathbf{x},\omega'\right) \\ \Rightarrow\ &\Pi(\mathbf{x},\omega) = \gamma_l(\mathbf{x},\omega)\Phi_{lm}(\omega)\gamma_m^*(\mathbf{x},\omega). \end{aligned} \quad (12)$$

where $\langle\widetilde{p}(\mathbf{x},\omega)\widetilde{p}^*(\mathbf{x},\omega')\rangle$ refers to the ensemble average or mean value, and $\Phi_{lm}(\mathbf{x},\omega)$ is the cross spectral density between the integrated pressure force on the l^{th} and m^{th} elements.

Equation (12) is a handy expression for the power spectral density of the radiated sound pressure. It is given in terms of the derivative of the Green's function on the surface Σ at the centre of the individual surface elements and the cross spectral density matrix $\Phi_{lm}(\omega)$. The former can be calculated analytically in some cases (see below) or numerically if required. The latter can be calculated in the CFD by defining the surface elements and extracting the integrated pressure force on those elements as a time series. It is then a straightforward matter to calculate the cross spectral density. These quantities contain exactly enough information to calculate the far-field sound pressure level. By integrating over the (relatively large) "acoustic" elements, i.e. elements whose size is determined by acoustic length scales rather than flow length scales, substantial reductions in the amount of data that need to be stored from the CFD may be achieved with no penalty in the accuracy of the acoustic prediction.

The size of the elements is determined only by the restrictions imposed by the shortest wavelength. In the event

that elements are large compared to their curvature so that variations in $\mathbf{n}$ cannot be ignored then equation (9) can be written

$$\tilde{p}(\mathbf{x},\omega) \approx \sum_l \int_{\Sigma_l} \tilde{P}(\mathbf{y},\omega)\, n_j(\mathbf{y})\, \mathrm{d}^2\mathbf{y} \times \frac{\partial g}{\partial y_j}\left(\mathbf{x},\mathbf{y}^l,\omega\right) = \mathbf{f}^l(\omega)\cdot\boldsymbol{\gamma}^l(\mathbf{x},\omega) \tag{13}$$

where

$$\mathbf{f}^l(\omega) = \sum_l \int_{\Sigma_l} \tilde{P}(\mathbf{y},\omega)\, n_j(\mathbf{y})\, \mathrm{d}^2\mathbf{y}$$
$$\boldsymbol{\gamma}^l(\mathbf{x},\omega) = \sum_l \frac{\partial g}{\partial y_j}\left(\mathbf{x},\mathbf{y}^l,\omega\right). \tag{14}$$

For the same number of elements, this expression clearly requires more storage than the simpler equation (12), but allowing for curvature of the elements permits a much more efficient discretization of the surface. In some cases, the entire surface may be small enough to take as a single element, in which case $\tilde{p}(\mathbf{x},\omega) \approx \mathbf{f}(\omega)\cdot\boldsymbol{\gamma}(\mathbf{x},\omega)$ is obtained, where $\mathbf{f}$ is the total fluctuating force on the surface and $\boldsymbol{\gamma}$ is the gradient of the Green's function evaluated at the geometrical centre of the surface. Surfaces that are compact in one direction, but not in another, such as a long narrow cylinder, may also benefit from this approach.

4. Application to a circular cylinder

In this section some of the foregoing theory on a simple example is demonstrated, the flow past a circular cylinder. A rigid circular cylinder of diameter D and length $L = 2.3D$ is placed with the ends at $(0,0,-L/2)$ and $(0,0,L/2)$, normal to a steady uniform flow of speed $(U,0,0)$, Figure 1. The cylinder is so short that it is compact in the spanwise direction (z-direction); that is, the length of the cylinder, L, is smaller than the wavelength, λ; and the flow is correlated. Here there are no surfaces in addition to the compact surface that generates the noise so the Green's function is simply the free-space Green's function

$$g(\mathbf{x},\mathbf{y},\omega) = \frac{\mathrm{e}^{-\mathrm{i}k|\mathbf{x}-\mathbf{y}|}}{4\pi|\mathbf{x}-\mathbf{y}|} \tag{15}$$

$$\frac{\partial g(\mathbf{x},\mathbf{y},\omega)}{\partial y_j} = \frac{\left(x_j - y_j\right)}{|\mathbf{x}-\mathbf{y}|}\left[\mathrm{i}k + \frac{1}{|\mathbf{x}-\mathbf{y}|}\right]\frac{\mathrm{e}^{-\mathrm{i}k|\mathbf{x}-\mathbf{y}|}}{4\pi|\mathbf{x}-\mathbf{y}|}. \tag{16}$$

If the entire cylinder surface is compact and located about the origin then

$$\boldsymbol{\gamma}(\mathbf{x},\omega) = \frac{\partial g(\mathbf{x},\mathbf{0},\omega)}{\partial y_j} = \frac{x_j}{|\mathbf{x}|}\left[\mathrm{i}k + \frac{1}{|\mathbf{x}|}\right]\frac{\mathrm{e}^{-\mathrm{i}k|\mathbf{x}|}}{4\pi|\mathbf{x}|} \approx \mathrm{i}k\frac{x_j}{|\mathbf{x}|}\frac{\mathrm{e}^{-\mathrm{i}k|\mathbf{x}|}}{4\pi|\mathbf{x}|} \tag{17}$$

in the far-field when $k|\mathbf{x}| \gg 1$. The fluctuating force can be divided into a drag and lift component and can be written as $\mathbf{f}(\omega) = \Delta(\omega)\mathbf{e}_1 + \Lambda(\omega)\mathbf{e}_2$, where $\Delta(\omega)$ and $\Lambda(\omega)$ are the Fourier transform of the drag and lift force

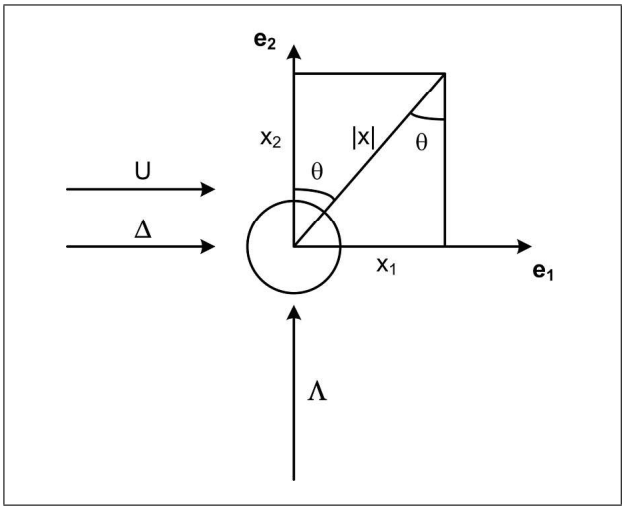


Figure 1. Drag and lift forces acting on the cylinder.

respectively. Therefore, particularizing equation (13) to the cylinder, the fluctuating acoustic pressure at position $\mathbf{x} = (x_1, x_2, 0)$ at a frequency ω is given by

$$\tilde{p}(\mathbf{x},\omega) \approx \mathrm{i}k\sin\theta\frac{\mathrm{e}^{-\mathrm{i}k|\mathbf{x}|}}{4\pi|\mathbf{x}|}\Delta(\omega) + \mathrm{i}k\cos\theta\frac{\mathrm{e}^{-\mathrm{i}k|\mathbf{x}|}}{4\pi|\mathbf{x}|}\Lambda(\omega). \tag{18}$$

The far-field power spectral density of the acoustic pressure turns to be

$$\Pi(\mathbf{x},\omega) = \left\langle\widetilde{p}(\mathbf{x},\omega)\widetilde{p}^*(\mathbf{x},\omega)\right\rangle = \frac{k^2\sin^2\theta}{16\pi^2|\mathbf{x}|^2}\langle\Delta(\omega)\Delta^*(\omega)\rangle + \frac{k^2\cos^2\theta}{16\pi^2|\mathbf{x}|^2}\langle\Lambda(\omega)\Lambda^*(\omega)\rangle + \frac{k^2\sin\theta\cos\theta}{16\pi^2|\mathbf{x}|^2}\left[\langle\Delta(\omega)\Lambda^*(\omega)\rangle + \langle\Lambda(\omega)\Delta^*(\omega)\rangle\right], \tag{19}$$

where $\langle\Delta(\omega)\Delta^*(\omega)\rangle$ is the power spectral density of the drag force, $\langle\Lambda(\omega)\Lambda^*(\omega)\rangle$ is the power spectral density of the lift force, and $\langle\Delta(\omega)\Lambda^*(\omega)\rangle$ and $\langle\Lambda(\omega)\Delta^*(\omega)\rangle$ are the cross power spectral densities between the drag and lift forces.

As the drag and lift forces are uncorrelated, the cross terms drop down and it turns

$$\Pi(\mathbf{x},\omega) = \left\langle\widetilde{p}(\mathbf{x},\omega)\widetilde{p}^*(\mathbf{x},\omega)\right\rangle = \frac{k^2\sin^2\theta}{16\pi^2|\mathbf{x}|^2}\langle\Delta(\omega)\Delta^*(\omega)\rangle + \frac{k^2\cos^2\theta}{16\pi^2|\mathbf{x}|^2}\langle\Lambda(\omega)\Lambda^*(\omega)\rangle. \tag{20}$$

Taking into account that the lift component dominates equation (20) becomes

$$\Pi(\mathbf{x},\omega) = \left\langle\widetilde{p}(\mathbf{x},\omega)\widetilde{p}^*(\mathbf{x},\omega)\right\rangle = \frac{k^2\cos^2\theta}{16\pi^2|\mathbf{x}|^2}\langle\Lambda(\omega)\Lambda^*(\omega)\rangle. \tag{21}$$

For high frequencies the cylinder surface is no longer compact and it is divided into elements. Taking sufficiently many flat elements to resolve the surface, equation (12) may be used.

5. Results and discussion

5.1. CFD computational details

The computational domain used to simulate the flow around a circular cylinder with a diameter D of 0.04m is shown in Figure 2. The length of the domain in the streamwise x-direction is $27D$, with the centre of the cylinder placed $4.5D$ downstream from the inlet; while in the lateral y-direction it is $9D$ long. A spanwise extent of the domain of $L = 2.3D$ has been considered. A uniform grid distribution has been set along both the lateral (y) and spanwise (z) directions, with 60 and 36 nodes respectively. In the radial direction around the cylinder, 50 nodes have been distributed according to a geometric ratio of 1.13, which allows a reduction of the element size when getting closer to the cylinder. After the square with a finer mesh around the cylinder, 150 nodes have been set in the streamwise x-direction. This grid distribution leads to a mesh of 756000 hexahedral cells.

Considering a Reynolds number of $\mathrm{Re} = 1.4 \cdot 10^5$, the average speed of the flow will be $U_\infty = 35\mathrm{m/s}$. A velocity inlet boundary condition with a uniform unperturbed streamwise velocity profile of 35m/s has been set at the upwind of the domain, $x = -4.5D$, whereas an outflow boundary condition is assumed at the outlet (downwind) section, $x = 22.5D$. Periodic boundary conditions have been specified in the spanwise z-direction, i.e. $z = -1.15D$ and $z = 1.15D$; and symmetry planes have been set on the lateral surfaces, i.e. $y = -4.5D$ and $y = 4.5D$. A non-slip wall boundary condition has been specified on the cylinder surface.

A Large Eddy Simulation (LES) turbulence model has been considered, assuming the Smagorinsky-Lilly subgrid-scale model with a constant of $C_s = 0.1$. A wall $y+$ (wall-adjacent cell's centroid placement) between $y+ = 0.45 - 12$ is obtained on the cylinder wall. The mesh is fine enough to resolve the laminar sublayer in most of the cylinder surface, $y+ < 5$, and the near-wall treatment considered in LES turbulence model allows to obtain the wall shear stress from the laminar stress-strain relationship, the wall function $U+ = y+$ satisfied in the laminar sublayer is applied. Values for $y+$ higher than 5 are obtained where the boundary layer separation occurs, but even though, the separation angle is well predicted. When the mesh is too coarse to resolve the laminar sublayer, it is assumed that the centroid of the wall-adjacent cell falls within the logarithmic region of the boundary layer, and the law-of-the-wall is employed. The flow is assumed to be incompressible.

Many calculation schemes are sensitive to the computational time and space intervals (Δt, Δx) used. The Courant-Friedrichs-Lewy number expresses the ratio of the distance travelled by a disturbance in one time step to the length of a computational distance step, that is, it is necessary that a fluid particle moves only a fraction of the grid spacing Δx in a time step Δt. A time step of $\Delta t = 10^{-5}\mathrm{s}$ is assumed, which ensures a Courant-Friedrichs-Lewy number of $CFL < 1$ and therefore, the stability of the numerical method [30, 10] but also the Δt to be the same order as the smallest turbulent scales being resolved.

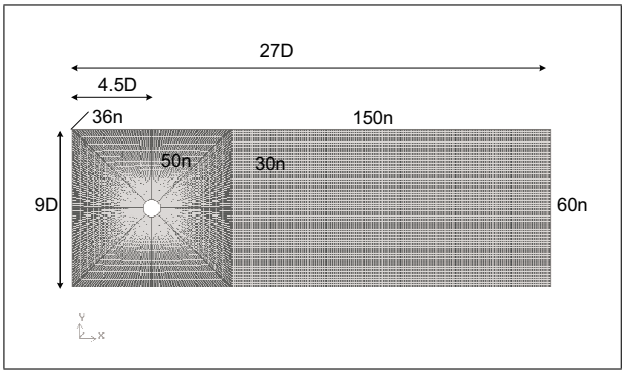


Figure 2. Computational domain and grid size.

After Reynolds-Averaged Navier-Stokes (RANS) simulation considering $\kappa - \epsilon$ RNG (Renormalization Group Method) viscous model, the LES simulation has been run during 10 vortex shedding cycles before starting the statistical averaging. The time averaged (mean) of the instantaneous values and the root-mean-squares of the fluctuating values have been sampled during 20 shedding cycles. Samples of each of time step have been taken into account.

5.2. CFD results

Before discussing the acoustic results, the CFD simulation will be validated. Table I shows the Strouhal number St, the mean drag coefficient C_D, the r.m.s. (root-mean-square) lift coefficient $C_{L'}$, the mean back pressure coefficient C_{pb}, and the mean separation angle θ_{sep}.

The present LES results have been compared with LES results obtained by Breuer [31] and Tremblay [32], and Detached Eddy Simulation (DES) results given by Travin *et al.* [33]. Parameters obtained with the present LES simulation are within the range predicted by Travin *et al.* [33] with the DES simulation. The mean drag coefficient and the mean back pressure coefficient agree with the values given by the other LES simulations, whereas the mean separation angle differs.

The present LES predicts a St number of 0.23. The Strouhal number St corresponding to a Reynolds number of $\mathrm{Re} = 1.4 \cdot 10^5$ given by Norberg [34] is between 0.18 and 0.192. Cantwell and Coles [35] determined a Strouhal number of $\mathrm{St} = 0.179$ in their experiment, but acknowledged it to be slightly lower than the consensus of other experiments. In the literature, when $\mathrm{Re} = \mathrm{O}(10^5)$ the generally accepted value for the Strouhal number is $\mathrm{St} \approx 0.2 - 0.21$, as shown by Wieselsberger *et al.* [36], Achenbach [37], Son and Hanratty [38], Zdravkovich [39], Fey et al. [40] and Roshko [41]. The computed mean drag coefficient is underpredicted in this simulation. The mean pressure coefficient at the back of the cylinder agrees fairly well with the experimental data.

The separation angle is the angle from the forward stagnation point at which the boundary layer separates giving

Table I. Integral flow parameters from LES and DES simulations and experiments at Re = $1.4 \cdot 10^5$.

	St	C_D	$C_{L'}$	C_{pb}	θ_{sep}
Simulation					
LES-Present	0.23	0.92	0.32	-1.02	78.54°
LES-Breuer [31]	-	1.22-1.45	-	-1.40,-1.76	92.6°-96.4°
LES H1-Tremblay [32]	-	1.134	-	-1.22	90°
LES H2-Tremblay [32]	-	0.937	-	-0.98	90°
LES H3-Tremblay [32]	-	1.27-1.45	-	-	96.7°
DES-Travin *et al.* [33]	-	0.87-1.08	-	-0.81,-1.04	77.78°
Experiments					
Norberg [34, 42]	0.18-0.192	-	0.5	-	-
Cantwell and Coles [35]	0.179	1.237	-	-1.21	77°
Wieselsberger *et al.* [36], Achenbach [37], Son and Hanratty [38], Zdravkovich [39], Fey *et al.* [40], Roshko [41]	$\approx 0.2 - 0.21$	≈ 1.2	-	-	72-78°
Fujino *et al.* [43]	-	-	0.06-0.3	-	-
Humphreys [44]	-	-	0.2-0.5	-	-
Weaver [45]	-	-	0.1-0.2	-	-
Bublitz [46]	-	-	0.02-0.07	-	-
Schewe [47]	-	-	0.01-0.38	-	-
Cheung and Melbourne [48]	-	-	0.04-0.46	-	-
Watanabe *et al.* [49]	-	-	0.06-0.51	-	-

rise to wake structures in the downstream of the cylinder flow. The location of the separation angle also corresponds to the point at which $\partial u/\partial y = 0$ when plotting the mean wall shear stress on the cylinder surface. The LES simulation predicts a value of $\theta_{sep} = 78.54°$. Cantwell and Coles [35] provided a mean separation point (which was identified with the inflection point for the mean pressure coefficient) of about $\theta_{sep} = 77°$. Achenbach [37] found that for a sub-critical flow, Re $= 10^5$, the boundary layer is still laminar and the separation point occurs at $\theta_{sep} = 78°$, while the minimum for the separation angle $\theta_{sep} = 72°$ occurred at Re $= 1.5 \times 10^5$. The experimental investigation by Son and Hanratty [38] determined a value of $\theta_{sep} = 78°$ at Re $= 10^5$.

For the r.m.s (root-mean-square) lift coefficient Norberg [34, 42] obtained a value of about 0.5. The experimental lift data provided by Norberg only contains sectional or near-sectional lift coefficients for a short spanwise segment of length l_c on a cylinder of length l, while in the present simulation, the total fluctuating lift coefficient acting on the entire cylinder is obtained, giving a value of $C_{L'} = 0.32$. For Reynolds numbers between $8 \cdot 10^4$ and $60 \cdot 10^4$ Fujino *et al.* [43] measured a total lift coefficient between 0.06 and 0.3, while Humphreys [44] obtained a lift coefficient of $0.2 - 0.5$ for Reynolds numbers between $3 \cdot 10^4$ and $57 \cdot 10^4$ in his measurements. A similar behaviour in the total fluctuating lift coefficient on the whole cylinder is measured by Weaver [45], Bublitz [46], Schewe [47], Cheung and Melbourne [48] and Watanabe *et al.* [49].

A critical remark should be included at this point regarding the comparison of predicted results and experimental measurements. Cantwell and Coles mention [35] that the end conditions for the cylinder model have a critical influence in the flow, but there are also several other influencing factors, such as the Reynolds number, the aspect ratio L/D of the cylinder, the blockage ratio D/H of the cylinder in the wind tunnel, the roughness of the cylinder, the free-stream turbulence level and the Mach between others. But experimental data are still useful to somehow validate the predicted values.

For a more detailed validation of the time-averaged flow field, profiles of the velocity components, Reynolds stresses and pressure coefficient have been compared with experimental data given by Cantwell and Coles [35], results can be found in [50].

5.3. Acoustic results

The sound pressure level spectrum L_p predicted using equations (12) and (21) is shown in Figure 3 for a resolution of 8 Hz at 1 m above the cylinder. The solid gray line corresponds to equation (12) based on force time series on a discretized surface acoustic mesh on the cylinder, while the dashed black line represents equation (21) considering the lift coefficient on the cylinder surface. Both methods are able to predict the peak value at a frequency of 213.3 Hz, which corresponds to the vortex shedding frequency given by the Strouhal number St = 0.23. Strouhal [51] found that the frequency of the tone was identical to the vortex shedding frequency. This phenomenon is also known as the Aeolian tone.

Holle [52] shows how the frequency of the aeolian tone decreases as the diameter of the cylinder increases, for a flow speed of 35 m/s and a diameter of the cylinder of 0.0195 m, the frequency of the main tone is 250 Hz. In the present simulation, for the same flow speed and a diameter of the cylinder of 0.04 m, a frequency of 213.3 Hz is ob-

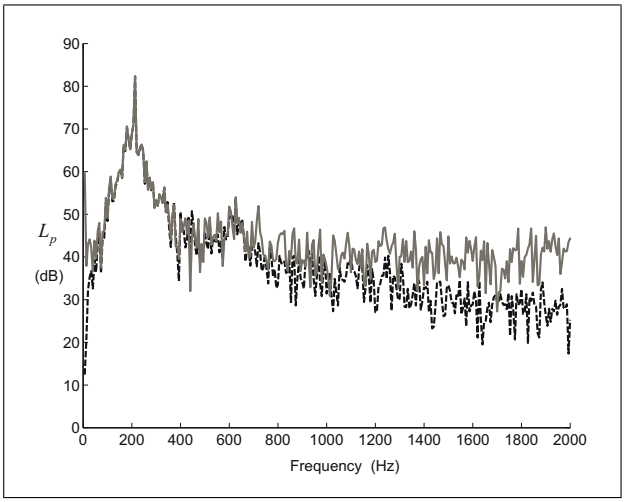


Figure 3. Sound pressure level at receiver position [0 1 L/2] at a resolution of 8 Hz: Calculated using equation (12) (solid gray line) and using equation (21) (dashed black line).

Table II. Overall sound pressure level by use of different equations.

Equation (12)	Equation (21)	Phillips Equation
84.3 dB	84.0 dB	85.0 dB

tained for the aeolian tone, which is in agreement with the behaviour shown by Holle.

The difference by using equations (12) and (21) for broadband noise in the higher frequency region could be explained considering that the approach leading to equation (21) works with integral magnitudes, such as the lift force, and this integration might act as a filter reducing the contribution of the highest frequencies to the frequency spectrum. Furthermore, at high frequencies the cylinder surface is no longer compact and it must be divided into elements. Considering sufficiently many flat elements to resolve the surface, equation (12) is more suitable for high frequencies.

Table II shows the overall sound pressure level obtained with the power spectral densities given by equations (12) and (21), and compared with the value given by the Phillips equation [53]. Phillips carried out an experiment with two thin wires, 60 cm in length and 0.0123 cm in diameter, held between two side arms mounted on a spinning shaft. Even if side walls are needed in the experiment, the purpose of using such long cylinders is to avoid end effects. He mentions that the axial length scale of the force fluctuations when $100 < \mathrm{Re} < 160$ is approximately $17D$, and within this range of the Reynolds number a factor of 0.27 should be used in Phillips equation for the mean square acoustic pressure. He also describes that in the turbulent flow near a cylinder at Reynolds numbers of the order $5 \cdot 10^3$ the integral length scale of the eddies along the axis is about $3D$.

The Reynolds number in the present simulation is $\mathrm{Re} = 1.4 \cdot 10^5$, and periodic boundary conditions have been specified in the spanwise z-direction in order to avoid end effects. The length of the domain in the spanwise z-direction is $2.3D$, and taking into account that the Reynolds number is also higher than $5 \cdot 10^3$, this length is enough to cover the length scale of the eddies. The length of $2.3D$ in the spanwise z-direction is also in agreement with the case studied in the ESPRIT project ALESSIA [54]. Furthermore, it has been checked that the forces on the cylinder surface are longitudinally correlated.

Phillips found that the mean square acoustic pressure generated by the cross-flow around a cylinder at high Reynolds numbers, when the cylinder wake is turbulent, to be

$$\overline{p'^2(r)} \approx 0.037 \cos^2\theta \frac{\rho_0^2 L D U^6 \mathrm{St}^2}{c_0^2 r^2}, \qquad (22)$$

where θ is the angle between the direction of observation and the incident stream, ρ_0 is the density, L is the length of the cylinder, D is the diameter of the cylinder, U is the flow speed, St is the Strouhal number, c_0 is the speed of sound and r is the distance from the cylinder. The numerical factor changes to 0.037 in the expression for the mean square acoustic pressure, the reason for this numerical factor to be considerably reduced for high Reynolds numbers is the reduced length scale of the fluctuations in lift per unit length. The Phillips equation is therefore based only on some geometrical and flow parameters, and its comparison with previous experimental data by Holle [52] and Gerrard[55] gives a very good agreement.

Equation (12) based on the force time series provides an overall sound pressure level of 84.3 dB, while equation (21) based on the lift coefficient gives 84.0 dB. Both equations, compared to the experimental value given by Phillips, 85.0 dB, provide a slightly lower value, but still rather good agreement is obtained.

Finally, the directivity of the sound field given by equations (12) and (20) has been compared. Even if it is enough considering the lift force to get the sound pressure level spectrum and the overall sound pressure level (equation (21)), the drag force needs to be taken into account in order to obtain properly the directivity pattern of the sound field, and equation (20) has to be considered instead of equation (21). Figures 4 and 5 compare the overall sound pressure level directivity pattern at 1 m from the cylinder obtained with equations (12) and (20), with a resolution of 8 Hz, and for the lift and drag component respectively.

The lift force is the predominant sound source, and it radiates like a dipole with the maximum radiation upwards ([0 1 0]) and downwards ([0 -1 0]) the cylinder, getting the main peak at 213.3 Hz. On the other hand, when the receiver or observation point is placed behind ([1 0 0]) or before ([-1 0 0]) the cylinder, these observation points are placed at a zero of the radiation pattern of the lift force, but at a position of maximum radiation of the drag force, getting the main peak at 426.6 Hz, which is twice the frequency. Summarizing, both mechanisms have figure-of-eight directivities with the maxima in perpendicular directions. Curle [56] extended Lighthill's [4] analogy to

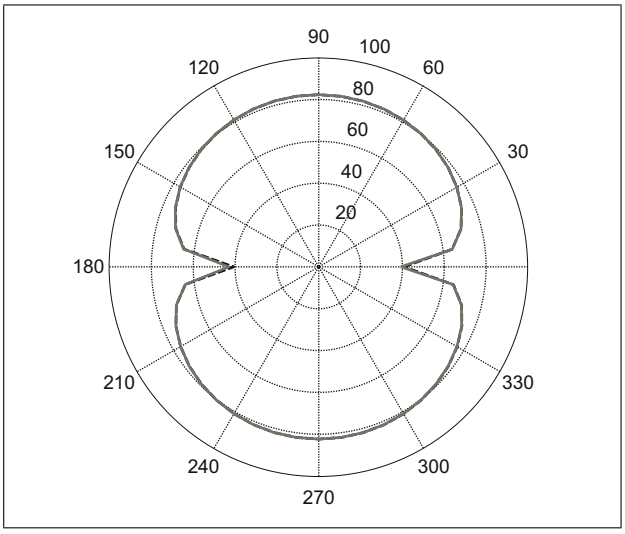


Figure 4. Overall sound pressure level directivity patterns at 1 m from the cylinder considering lift force: equation (12) (solid gray line), equation (20) (dashed black line).

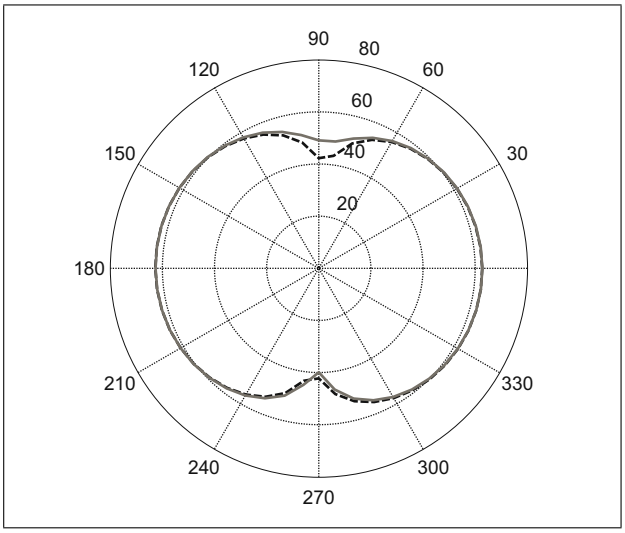


Figure 5. Overall sound pressure level directivity patterns at 1 m from the cylinder considering drag force: equation (12) (solid gray line), equation (20) (dashed black line).

bounded flows, showing that the surface pressure fluctuations around the body lead to a dipole-like acoustic field. Gerrard [55], Phillips [53] and Etkin *et al.* [57] confirmed experimentally that the Aeolian tone has a directivity normal to the f luid stream and is closely related to the lift force.

6. Conclusions

A versatile framework to treat compact sources by replacing them with the source distributions using the Ffowcs Williams-Hawkings formulation has been introduced, where the pressure on the surface is evaluated using commercial CFD codes. In this paper, the approach has been applied to a free-field application where the surface is compact and the analytical free-space Green's function may be used.

This approach reproduces accurately the vortex shedding frequency which agrees with the Strouhal number obtained experimentally. Furthermore, the overall sound pressure level predicted is in keeping with the experimental data.

The requirements in data storage and transfer are significantly reduced by using this method; compared to a usual acoustic simulation combining CFD and acoustic codes, the total size of the input files for the acoustic computation has been reduced by a factor of 23. Besides, if the flow remains essentially the same, the CFD simulation should not need to be repeated in case different acoustic scenarios should be studied.

Acknowledgments

The support of the European Community (contract No: MEST-CT-2004-503675) under a Marie Curie Host Fellowship for Early Stage Researchers Training is gratefully acknowledged. The research training was carried out in Ørsted Department, section for Acoustic Technology, at the Technical University of Denmark (DTU), within the framework of the European Doctorate in Sound and Vibration Studies (EDSVS). After the Marie Curie Fellowship, this research work has been financed by the Ministry of Education of Spain within the framework of Torres Quevedo Programme and co-financed by the European Social Fund.

References

[1] T. Colonius, S. K. Lele, P. Moin: Sound generation in a mixing layer. Journal of Fluid Mechanics **330** (1997) 375–409.

[2] O. Inoue, N. Hatakeyama: Sound generation by a two-dimensional circular cylinder in a uniform flow. Journal of Fluid Mechanics **471** (2002) 285–314.

[3] J. B. Freund, S. K. Lele, P. Moin: Numerical simulation of a Mach 1.92 turbulent jet and its sound field. AIAA JOURNAL **38** (2000) 2023–2031.

[4] M. J. Lighthill: On sound generated aerodynamically. Part I: General theory. Proceedings of the Royal Society of London (1952) 564–587.

[5] M. J. Lighthill: On sound generated aerodynamically. Part II: Turbulence as a source of sound. Proceedings of the Royal Society of London (1954) 1–32.

[6] M. S. Howe: Contributions to the theory of aerodynamic sound, with application to excess jet noise and the theory of the flute. Journal of Fluid Mechanics **71** (1975) 625–673.

[7] X. Gloerfelt, C. Bailly, D. Juvé: Direct computation of the noise radiated by a subsonic cavity flow and application of integral methods. Journal of Sound and Vibration **266** (2003) 119 – 146.

[8] U. Piomelli: Wall-layer models for large-eddy simulations. Progress in Aerospace Sciences **44** (2008) 437 – 446.

[9] P. Moin: Advances in large eddy simulation methodology for complex flows. International Journal of Heat and Fluid Flow **23** (2002) 710 – 720.

[10] S. B. Pope: Turbulent flows. Cambridge University Press, Cambridge, 2000.

[11] B. J. Boersma, S. K. Lele: Large eddy simulation of compressible turbulent jets. Annual Research Briefs Center for Turbulence Research, Stanford University and NASA - Ames Research Center, 1999.

[12] C. Bogey, C. Bailly, D. Juvé: Noise investigation of a high subsonic, moderate Reynolds number jet using a compressible large eddy simulation. Theoretical and Computational Fluid Dynamics **16** (2003) 273–297.

[13] N. Andersson, L.-E. Eriksson, L. Davidson: Investigation of an isothermal mach 0.75 jet and its radiated sound using large-eddy simulation and kirchhoff surface integration. International Journal of Heat and Fluid Flow **26** (2005) 393 – 410.

[14] D. J. Bodony, S. K. Lele: Current status of jet noise predictions using large-eddy simulation. AIAA Journal **46** (2008) 364–380.

[15] T. Takaishi, M. Miyazawa, C. Kato: A computational method of evaluating noncompact sound based on vortex sound theory. The Journal of The Acoustical Society of America **121(3)** (2006) 1353–1361.

[16] J. Boudet, D. Casalino, M. Jacob, P. Ferrand: Prediction of sound radiated by a rod using large eddy simulation. AIAA-Paper (2003) 3217.

[17] X. Gloerfelt, F. Pérot, C. Bailly, D. Juvé: Flow-induced cylinder noise formulated as a diffraction problem for low Mach numbers. Journal of Sound and Vibration **287** (2005) 129–151.

[18] W. Béchara, P. Lafon, C. Bailly, S. M. Candel: Application of a $\kappa - \epsilon$ turbulence model to the prediction of noise for simple and coaxial free jets. The Journal of the Acoustical Society of America **97** (1995) 3518–3531.

[19] C. Bailly, S. Candel, P. Lafon: Prediction of supersonic jet noise from a statistical acoustic model and a compressible turbulence closure. Journal of Sound and Vibration **194** (1996) 219 – 242.

[20] C. Bailly, P. Lafon, S. Candel: Subsonic and supersonic jet noise predictions from statistical source models. AIAA Journal **35** (1997) 1688–1696.

[21] A. Khavaran: Role of anisotropy in turbulent mixing layer. AIAA Journal **37** (1999) 832–841.

[22] P. Huerre, P. A. Monkewitz: Local and global instabilities in spatially developing flows. Annual Review of Fluid Mechanics **22** (1990) 473–537.

[23] L. Brevdo, T. J. Bridges: Local and global instabilities of spatially developing flows: cautionary examples. Proceedings of the Royal Society of London. Series A: Mathematical, Physical and Engineering Sciences **453** (1997) 1345–1364.

[24] D. G. Crighton, P. Huerre: Shear-layer pressure fluctuations and superdirective acoustic sources. Journal of Fluid Mechanics Digital Archive **220** (1990) 355–368.

[25] X. Wu, P. Huerre: Low-frequency sound radiated by a nonlinearly modulated wavepacket of helical modes on a subsonic circular jet. Journal of Fluid Mechanics **637** (2009) 173–211.

[26] M. S. Howe: Acoustics of fluid-structure interactions. Cambridge Monographs on Mechanics. Cambridge University Press, Cambridge, 2008.

[27] P. A. Nelson, C. L. Morfey: Aerodynamic sound production in low speed flow ducts. Journal of Sound and Vibration **79** (1981) 263–289.

[28] A. Hirschberg, S. W. Rienstra: An introduction to acoustics. Available at www.win.tue.nl/ $\sim$ sjoerdr/papers/boek.pdf, 2008.

[29] D. G. Crighton, A. P. Dowling, J. E. Ffowcs Williams, M. Heckl, F. G. Leppington: Modern methods in analytical acoustics - lecture notes. Springer-Verlag, Great Britain, 1992.

[30] V. Eswaran, S. B. Pope: An examination of forcing in direct numerical simulations of turbulence. Computers and Fluids **16** (1988) 257–278.

[31] M. Breuer: A challenging test case for large eddy simulation: high Reynolds number circular cylinder flow. International Journal of Heat and Fluid Flow **21** (2000) 648–654.

[32] F. Tremblay: Direct and large-eddy simulation of flow around a circular cylinder at subcritical Reynolds numbers. Dissertation. Technical University of Munich, 2001.

[33] A. Travin, M. Shur, M. Strelets, P. Spalart: Detached-eddy simulations past a circular cylinder. Flow, Turbulence and Combustion **63** (2000) 293–313.

[34] C. Norberg: Flow around a circular cylinder: aspects of fluctuating lift. Journal of Fluids and Structures **15** (2001) 459–469.

[35] B. Cantwell, D. Coles: An experimental study of entrainment and transport in the turbulent near wake of a circular cylinder. Journal of Fluid Mechanics **136** (1983) 321–374.

[36] C. Wieselsberger, A. Betz, L. Prandtl: Versuche über den Widerstand gerundeter und kantiger Körper (Experiments on the resistance of rounded and edged bodies). Ergebnisse AVA Göttingen (1923) 22–32.

[37] E. Achenbach: Distribution of local pressure and skin friction around a circular cylinder in cross-flow up to $Re = 5x10^6$. Journal of Fluid Mechanics **34(4)** (1968) 625–639.

[38] J. S. Son, T. J. Hanratty: Velocity gradients at the wall for flow around a cylinder at Reynolds numbers from $5x10^3$ to 10^5. Journal of Fluid Mechanics **35(2)** (1969) 353–368.

[39] M. M. Zdravkovich: Flow around circular cylinders, vol. 1: Fundamentals. Oxford Science Publications. Oxford University Press, USA, 1997.

[40] U. Fey, M. König, H. Eckelmann: A new Strouhal-Reynolds number relationship for the circular cylinder in the range $47 < Re < 2x10^5$. Physics of Fluids **10(7)** (1998) 1547–1549.

[41] A. Roshko: On the development of turbulent wakes from vortex streets. Report for the National Advisory Committee for Aerodynamics 1191, NACA, 1954.

[42] C. Norberg: Fluctuating lift on a circular cylinder: review and new measurements. Journal of Fluids and Structures **17** (2003) 57–96.

[43] T. Fujino, T. Takahei, K. Nakagawa, Y. Arita: The dynamic behavior of tall stacks under the action of wind. Proceedings 7th Japan National Congress for Applied Mechanics, University of Tokyo, 1958, 387–392.

[44] J. S. Humphreys: On a circular cylinder in a steady wind at transition Reynolds numbers. Journal of Fluid Mechanics **9** (1960) 603–612.

[45] W. Weaver: Wind-induced vibrations in antenna members. ASCE Journal of the Engineering Mechanics Division **87** (1961) 141–165.

[46] P. Bublitz: Unsteady pressures and forces acting on an oscillating circular cylinder in transverse flow. Naudascher, E. (Ed.), IUTAM-IAHR Flow-Induced Structural Vibrations. Symp. Karlsruhe, Springer, Berlin, 1972, 443–453.

[47] G. Schewe: On the force fluctuations acting on a circular cylinder in crossflow from subcritical up to transcritical Reynolds numbers. Journal of Fluid Mechanics **133** (1983) 265–285.

[48] J. C. K. Cheung, W. H. Melbourne: Turbulence effects on some aerodynamic parameters of a circular cylinder at supercritical Reynolds numbers. Journal of Wind Engineering and Industrial Aerodynamics **14** (1983) 399–410.

[49] H. Watanabe, A. Ihara, H. Hashimoto: Hydraulic characteristics of a circular cylinder with a permeable wall. JSME International Journal **39** (1996) 482–488.

[50] A. Pradera, G.Keith, F. Jacobsen, N. Gil-Negrete, A. Rivas: A numerical study of fluid flow past a circular cylinder at Re=3900 and a practical approach to noise prediction. Proceedings of the 14th International Congress on Sound and Vibration, ICSV14, Cairns, Australia, 2007.

[51] V. Strouhal: Über eine besondere Art der Tonerregung (About a particular manner of tonal excitation). Annalen der Physik und Chemie (1878) 216–251.

[52] W. Holle: Frequenz- und Schallstärkemessungen an Hiebtönen (Frequency and acoustic power measurement on aeolian tones). Akustische Zeitschrift (1938) 321–331.

[53] O. M. Phillips: The intensity of aeolian tones. Journal of Fluid Mechanics **1** (1956) 607–624.

[54] E. project ALESSIA: Application of large-eddy simulation to the solution of industrial problems: Validation report. 2002.

[55] J. H. Gerrard: Measurements of the sound from circular cylinders in an air stream. Proceedings Physical Society (1955) 453–461.

[56] N. Curle: The influence of solid boundaries upon aerodynamic sound. Proceedings of the Royal Society of London (1955) 505–514.

[57] B. Etkin, G. K. Korbacher, R. T. Keefe: Acoustic radiation from a stationary cylinder in a fluid stream (Aeolian tones). The Journal of The Acoustical Society of America **29(1)** (1957) 30–36.